AIAA JOURNAL
Vol. 45, No. 5, May 2007

Nonlinear Analysis of Unsteady Flows in Multistage Turbomachines Using Harmonic Balance

Kivanc Ekici* and Kenneth C. Hall†
Duke University, Durham, North Carolina 27708-0300

DOI: 10.2514/1.22888

A harmonic balance technique for the analysis of two-dimensional linear (small-disturbance) and nonlinear unsteady flows in multistage turbomachines is presented. The present method uses a mixed time-domain/frequency-domain approach that allows one to compute the unsteady aerodynamic response of multistage machines to both blade vibration (the flutter problem) and wake interaction (the forced response problem). In general, the flowfield may have multiple excitation frequencies that are not integer multiples of each other, so that the unsteady flow is (sometimes) aperiodic in time. Using our approach, we model each blade row using a computational grid spanning a single blade passage. In each blade row, we store several subtime level solutions. For flows that are periodic in time, these subtime levels span a single time period. For aperiodic flows, the temporal period spanned by these subtime level solutions is sufficiently long to sample the relevant discrete frequencies contained in the aperiodic flow. In both cases, these subtime level solutions are related to each other through the time-derivative terms in the Euler or Navier–Stokes equations and boundary conditions; complex periodicity conditions connect the subtime levels within a blade passage, and interrow boundary conditions connect the solutions among blade rows. The resulting discretized equations, which are mathematically steady because time derivatives have been replaced by a pseudospectral operator in which the excitation frequencies appear as parameters, can be solved very efficiently using multigrid acceleration techniques. In this paper, we apply the technique to both flutter and wake-interaction problems and illustrate the influence of neighboring blade rows on the unsteady aerodynamic response of a blade row.

Nomenclature

$\mathcal{A}$	=	control volume
$\mathbf{A}_k$, $\mathbf{B}_k$	=	kth temporal Fourier coefficients
$\tilde{\mathbf{A}}_{nlm}$, $\mathbf{B}_{nlm}$	=	nlmth Fourier coefficients in time and space
B_1, B_2	=	number of blades in stator and rotor rows
c	=	chord
$\mathbf{D}$	=	pseudospectral operator
E	=	total energy
$\mathbf{E}$, $\mathbf{E}^{-1}$	=	discrete inverse Fourier and Fourier transformation matrices
$\mathbf{E}^{+}$	=	pseudoinverse of $\mathbf{E}$ transformation matrix
$\boldsymbol{F}$, $\boldsymbol{G}$	=	flux vectors
$\dot{f}$, $\dot{g}$	=	control surface velocity
G	=	blade-to-blade gap
h	=	total enthalpy
h_0	=	amplitude of plunging motion
j	=	$\sqrt{-1}$
K	=	number of discrete frequencies
M	=	number of subtime levels
N	=	nodal diameters
P_{exit}	=	exit static pressure
Pr_l	=	laminar Prandtl number
Pr_t	=	turbulent Prandtl number
$P_{t_{\text{abs}}}$	=	inlet absolute total pressure
p	=	pressure
R	=	radial location of the two-dimensional section
$\mathcal{S}$	=	control surface
$\boldsymbol{S}$	=	source vector
S_t	=	source term for turbulence model
$T_{t_{\text{abs}}}$	=	inlet absolute total temperature
t	=	time
U	=	relative inflow velocity
$\boldsymbol{U}$	=	vector of conservation variables
$\boldsymbol{U}^*$	=	vector of conservation variables in all subtime levels
$\tilde{\boldsymbol{U}}$	=	vector of Fourier coefficients
u, v	=	Cartesian velocities
V_R	=	rotor speed
x, y	=	Cartesian coordinates
α_{abs}	=	inlet absolute flow angle
γ	=	specific heat ratio
μ_l	=	dynamic laminar viscosity
μ_t	=	dynamic turbulent viscosity
ν	=	kinematic viscosity
$\tilde{\nu}$	=	working variable for Spalart–Allmaras turbulence model
ρ	=	density
σ	=	interblade phase angle
τ	=	pseudotime
τ_{xx}, τ_{xy}, etc.	=	viscous stresses
Ω	=	wheel speed
ω	=	excitation frequency

Presented as Paper 422 at the 44th AIAA Aerospace Sciences Meeting and Exhibit, Reno, Nevada, 9–12 January 2006; received 31 January 2006; revision received 22 November 2006; accepted for publication 27 January 2007.

*Research Associate, Department of Mechanical Engineering and Materials Science, Member AIAA.

†Julian Francis Abele Professor and Chairman, Department of Mechanical Engineering and Materials Science, Associate Fellow AIAA.

Introduction

TRADITIONALLY, investigators have used two main families of aerodynamic theories to model unsteady flows in turbomachinery: time-linearized theories [1,2] and nonlinear time-domain theories [3]. The time-linearized approach assumes that the unsteady disturbances are small compared with the mean flow, and are harmonic in time with frequency ω. These assumptions allow one to linearize the governing equations about a nonlinear steady or mean operating condition. The resulting linearized equations can be solved very efficiently. The main drawback for this technique is its inability to model dynamically nonlinear effects (effects that may be profound for some forced response and flutter problems). Time-accurate, time-domain solvers, on the other hand, do not rely on any assumptions

regarding the size of the unsteady disturbance. Therefore, time-domain solvers can model dynamically nonlinear unsteady flows. However, time-domain solvers tend to be computationally expensive, typically one or two orders of magnitude more expensive than the frequency-domain solvers. Furthermore, time-domain solvers are not well suited for use with adjoint sensitivity techniques, because the adjoint methods require that the entire time history of the flow computation be stored, which can be prohibitively expensive.

The need for efficient nonlinear unsteady flow solvers led investigators to develop efficient frequency-domain techniques (actually mixed time and frequency domain). Hall et al. [4,5] proposed the "harmonic balance" approach. Using this approach, the unsteady flow is assumed to be temporally and spatially periodic, a condition satisfied to a good approximation for many unsteady flows of interest. In his original approach, Hall [4] represented periodic unsteady flows by a Fourier series in time with frequencies that are integer multiples of the original excitation frequency. The dependent variables were the Fourier coefficients of the Fourier series for each of the conservation variables. These Fourier series were then inserted into the Euler equations, and the resulting expressions were "balanced," that is, the resulting expressions were expanded, and terms were collected frequency by frequency. For the Euler equations to be satisfied, each frequency component must vanish independently. The result is a set of coupled complex partial differential equations, one for each frequency retained in the model. Time derivatives in the nth equation were replaced by $j\omega n$. Because time does not appear explicitly, the harmonic balance equations could be solved as steady-state flow problems. The harmonic balance method proposed by Hall has some similarities to the SLiQ (steady, linear, quadratic) approach proposed by Giles [6], and the related harmonic analysis approach proposed by He and Ning [7] and Ning and He [8], but is more general than either of those methods.

The computational cost of the original form of the harmonic balance equations did not scale well with the number of harmonics in the model. Furthermore, the algebraic balancing does not work well with more complicated equations such as the Navier–Stokes equations with turbulence models. To eliminate these problems, Hall et al. [5] developed an improved version of the harmonic balance technique in which the dependent variables are the conservation variables stored at a number of subtime levels over one period. This approach is somewhat similar to the dual time step approach [9], except that in the harmonic balance method several time levels are stored, and one makes use of the temporal periodicity of the flow. In the dual time step approach, one marches the solution from one physical time level to the next. Within each of these time steps, a number of pseudotime steps are taken to improve the accuracy of the physical time stepping solution. In the harmonic balance technique, on the other hand, all physical time levels are computed simultaneously, with pseudotime-marching used to drive the solution to convergence. The various physical time levels are only coupled to one another through the periodic boundary conditions (blade-to-blade periodicity), and through a pseudospectral operator that approximates the time derivatives in the Euler or Navier–Stokes equations. The advantage of this modified harmonic balance approach is that the computational cost scales (nearly) linearly with the number of time levels retained in the model. Furthermore, use of the pseudospectral time derivative operator allows one to use a small number of time levels (or equivalent harmonics) to obtain quite accurate solutions. Also, the resulting equations are mathematically steady equations and, therefore, convergence acceleration techniques used to speed convergence of steady flow solvers may be applied.

A number of investigators have contributed to the development of the harmonic balance technique, or have used the technique to solve interesting physical problems. McMullen et al. [10,11] used a very similar approach to investigate the flow around a cylinder and a pitching airfoil. Nadarajah et al. [12] applied the technique to an adjoint based design code and found that the computational time was greatly reduced compared with their time-accurate code. Van der Weide et al. [13] used this technique for turbomachinery forced response computations, and showed that engineering accuracy can be obtained with as few as 11 subtime levels per blade passing. However, their formulation was only able to investigate geometries in which the number of rotor and stator blades were equal. Thomas et al. [14–17] used the harmonic balance technique to study the nonlinear aerodynamic effects on flutter and limit-cycle oscillations for airfoils and wings. Thomas et al. [18] also developed a discrete adjoint code for computing steady and unsteady aerodynamic design sensitivities for compressible viscous flows about airfoil configurations in which the nominal flow solver was based on a harmonic balance solution technique. Welch et al. [19] used the harmonic balance technique to accurately and efficiently solve the incompressible Navier–Stokes equations to model (pulsating) synthetic jets in quiescent crossflows and compared their results to hotwire data. A similar frequency-domain model of the Euler equations was developed by Breard [20] for investigating sound propagation and radiation of lined ducts. This resulted in a less expensive approach to the calculation of noise propagation about a mean flow.

In the work presented in the literature to date, the application of the harmonic balance method has been restricted to unsteady flows arising from a single excitation frequency (and its harmonics). However, a number of interesting flows may have multiple excitation frequencies that are nonintegral multiples of one another. For example, when turbomachinery blades vibrate in flutter, the unsteady flow clearly contains the blade vibratory frequency and integer multiples. However, the fluttering blade may also be subjected to forced response from wakes from neighboring blade rows. The frequencies of the wake crossing will, in general, be nonintegral with the flutter frequency, but may nevertheless influence the unsteady solution through nonlinear mechanisms. We show in this paper how such aperiodic flows may be modeled in multistage turbomachines within the harmonic balance framework. The present method has some similarities to the work of He et al. [21], but the latter assumes that the spatial harmonics of the time-averaged nonuniform flow in a blade row interacts with the unsteady disturbances in the neighboring blade row only through the deterministic stresses. However, no such assumption is made in the present method.

Governing Equations

To motivate the present multistage harmonic balance analysis, we describe how the method may be applied to the solution of the two-dimensional Navier–Stokes equations. Note, however, that although we analyze only two-dimensional flows in this paper, the method is equally applicable to three-dimensional Navier–Stokes equations.

Consider the two-dimensional Reynolds-averaged Navier–Stokes equations, written in relative frame of reference, which may be stationary or moving with a rotor speed. The Navier–Stokes equations written in strong conservation form in Cartesian coordinates are given by

$$\frac{\mathrm{d}}{\mathrm{d}t}\iint_{\mathcal{A}} \boldsymbol{U}\,\mathrm{d}\mathcal{A} + \int_{\mathcal{S}} [(\boldsymbol{F}-\boldsymbol{U}\dot{f}),(\boldsymbol{G}-\boldsymbol{U}\dot{g})]\cdot\mathbf{n}\,\mathrm{d}\mathcal{S} = \iint_{\mathcal{A}} \boldsymbol{S}\,\mathrm{d}\mathcal{A} \quad (1)$$

The vector of conservation variables, the flux vectors, and the source vector are given by

$$\boldsymbol{U} = \begin{bmatrix} \rho \\ \rho u \\ \rho v \\ \rho E \\ \rho\tilde{\nu} \end{bmatrix}, \qquad \boldsymbol{F} = \begin{bmatrix} \rho u \\ \rho u^2 + p - \tau_{xx} \\ \rho uv - \tau_{xy} \\ \rho uh - \tau_{xh} \\ \rho u\tilde{\nu} - \tau_{x\nu} \end{bmatrix}$$

$$\boldsymbol{G} = \begin{bmatrix} \rho v \\ \rho uv - \tau_{yx} \\ \rho v^2 + p - \tau_{yy} \\ \rho vh - \tau_{yh} \\ \rho v\tilde{\nu} - \tau_{y\nu} \end{bmatrix}, \qquad \boldsymbol{S} = \begin{bmatrix} 0 \\ 0 \\ 0 \\ 0 \\ S_t \end{bmatrix}$$

where the shear stresses are given by

$$\tau_{xx} = \frac{2}{3}(\mu_l + \mu_t)\left(2\frac{\partial u}{\partial x} - \frac{\partial v}{\partial y}\right), \qquad \tau_{xy} = (\mu_l + \mu_t)\left(\frac{\partial u}{\partial y} + \frac{\partial v}{\partial x}\right)$$

$$\tau_{yy} = \frac{2}{3}(\mu_l + \mu_t)\left(2\frac{\partial v}{\partial y} - \frac{\partial u}{\partial x}\right)$$

In addition, the term τ_{xh} in the energy equation is defined as

$$\tau_{xh} = \left[u\tau_{xx} + v\tau_{xy} + \left(\frac{\mu_l}{Pr_l} + \frac{\mu_t}{Pr_t}\right)\frac{\partial h}{\partial x}\right]$$

In the present study, the turbulent viscosity is modeled using the one-equation Spalart–Allmaras [22] model. This equation is written in strong conservation form and is the fifth equation in Eq. (1). In addition, the laminar viscosity is determined using Sutherland's law. The τ_{xv} term in the turbulence model equation is given by

$$\tau_{xv} = \frac{3}{2}(\mu_l + \rho\tilde{\nu})\frac{\partial \tilde{\nu}}{\partial x}$$

The remaining components of the shear stresses and terms in energy and turbulence model equations are defined similarly. For an ideal gas with a constant specific heat ratio, the pressure is related to the conservation variables by

$$p = (\gamma - 1)\rho\left[E - \frac{1}{2}(u^2 + v^2) + \frac{1}{2}V_R^2\right]$$

In addition, the total enthalpy is defined as

$$h = \frac{\rho E + p}{\rho} = \frac{\gamma}{\gamma - 1}\frac{p}{\rho} + \frac{1}{2}(u^2 + v^2) - \frac{1}{2}V_R^2$$

where the rotor speed is defined as $V_R = \Omega R$. The Navier–Stokes equations are nonlinear in the conservation variables, and so the equations will admit nonlinear solutions.

Flowfield Kinematics

The present method can be applied to multistage turbomachines with any number of blade rows. However, for simplicity, consider the case where two blade rows operate in close proximity to one another (stator and rotor). Because of the relative motion of the neighboring blade rows, the coordinate system for the stator frame will be different from the coordinate system of the rotor frame. These two coordinate systems are related to each other through

$$x' = x + \Delta x, \qquad y' = -\Omega R t + y \tag{2}$$

where primed coordinates are fixed to the stator frame, Δx is the axial gap between the stator and the rotor rows, and ΩR is the rotor speed. Because of this relative motion, the frequency and the interblade phase angle of the waves in one row will be different when viewed in the frame of reference of the other rows. Thus, the unsteady excitation will shift (also known as the so-called Doppler effect) and scatter into different modes.

A detailed discussion of the frequency shift and scattering mechanism for a three-dimensional time-linearized solver is given in Hall and Ekici [23]. In the case of nonlinear flows, the mechanism is very similar. For completeness, we briefly explain how the frequencies and the interblade phase angles are computed for nonlinear flows. In the absence of blade vibration or some other external forcing mechanism, the flow between the blade rows can be decomposed into a Fourier series in the tangential direction. The flow will have nodal diameters where

$$N = lB_1 + mB_2 \tag{3}$$

where l and m can take on all integer values. If the blade of the rotor, for example, also vibrates with frequency ω_0 and with k_0 nodal diameters (corresponding to a fixed interblade phase angle $\sigma_0 = 2\pi k_0/B_2$), then the flow may be decomposed into nodal diameters, i.e.,

$$N = nk_0 + lB_1 + mB_2 \tag{4}$$

where n, l, and m can take on all integer values. In the rotor frame of reference, the temporal frequency of the unsteadiness of a particular nodal diameter mode will be

$$\omega = n\omega_0 - lB_1\Omega \tag{5}$$

Similarly, in the stator frame of reference, the frequency is given by

$$\omega' = n\omega_0 + (nk_0 + mB_2)\Omega \tag{6}$$

These discrete frequencies represent the possible frequencies that will appear in the flow (absent any self-induced flow unsteadiness or subharmonics). Therefore, the flow in the rotor, for example, may be represented by the time series

$$\boldsymbol{U}(x, y, t) = \sum_n \sum_l \sum_m [\tilde{\mathbf{A}}_{nlm}(x)\cos(\omega_{nlm}t + N_{nlm}y/R) + \tilde{\mathbf{B}}_{nlm}(x)\sin(\omega_{nlm}t + N_{nlm}y/R)] \tag{7}$$

or more generally

$$\boldsymbol{U}(x, y, t) = \mathbf{A}_0(x, y) + \sum_{k=1}^{K}[\mathbf{A}_k(x, y)\cos(\omega_k t) + \mathbf{B}_k(x, y)\sin(\omega_k t)] \tag{8}$$

where now ω_k is the kth nonrepeated nonzero frequency [we take the absolute value of negative frequencies in Eqs. (5) and (6)] and $\mathbf{A}_k$ and $\mathbf{B}_k$ are the Fourier coefficients of mode k. Strictly speaking, a Fourier series is periodic in time. However, this temporal series will generally be aperiodic for nonzero ω_0.

In the present computational method, we store the conservation variables in each blade row at a number of subtime levels. Assembled together into one vector, these solutions are denoted by the vector $\boldsymbol{U}^*$; we denote the vector of Fourier coefficients by

$$\boldsymbol{U}^* = \begin{Bmatrix} \boldsymbol{U}_1 \\ \boldsymbol{U}_2 \\ \boldsymbol{U}_3 \\ \boldsymbol{U}_4 \\ \vdots \end{Bmatrix}, \qquad \tilde{\boldsymbol{U}} = \begin{Bmatrix} \mathbf{A}_0 \\ \mathbf{A}_1 \\ \mathbf{A}_2 \\ \vdots \\ \mathbf{B}_1 \\ \mathbf{B}_2 \\ \vdots \end{Bmatrix} \tag{9}$$

For temporally periodic flows, the Fourier coefficients can be determined from the subtime level solutions by a discrete Fourier transform. Conversely, the conservation variables at the subtime levels can be determined from the Fourier coefficients by the inverse discrete Fourier transform. These relations can be written in matrix form as

$$\tilde{\boldsymbol{U}} = \mathbf{E}^{-1}\boldsymbol{U}^* \tag{10}$$

$$\boldsymbol{U}^* = \mathbf{E}\tilde{\boldsymbol{U}} \tag{11}$$

Note $\mathbf{E}$ is a square matrix because the number of subtime levels is equal to the number of Fourier coefficients.

For aperiodic flows, the situation is slightly more complicated. The flow is no longer periodic. Nevertheless, one can still determine the Fourier coefficients from information at time sublevels. However, some care must be taken to ensure the aperiodic equivalent of Eqs. (10) and (11) are well conditioned. First, the "period" spanned by the time sublevels and their spacing must be such that the Fourier coefficients are observable. We typically use about 50% more time levels than the number of Fourier coefficients for aperiodic flows. Equation (11) is essentially unchanged, except that $\mathbf{E}$ is no longer square; it now has more rows than columns. Second, Eq. (10) is replaced by

$$\tilde{\boldsymbol{U}} = \mathbf{E}^{+}\boldsymbol{U}^{*} \tag{12}$$

Note that in our computational code, we store $\boldsymbol{U}^{*}$ as our working variable, and only compute $\tilde{\boldsymbol{U}}$ at the computational boundaries when applying periodic, far-field, and interrow connectivity boundary conditions.

Harmonic Balance Equations

Having described the kinematics of the flow, we now turn our attention to the development of the harmonic balance equations. In conservation form, ignoring for the moment grid deformation, the Navier–Stokes equations may be written as

$$\frac{\partial \boldsymbol{U}}{\partial t} + \frac{\partial \boldsymbol{F}}{\partial x} + \frac{\partial \boldsymbol{G}}{\partial y} = \boldsymbol{S} \tag{13}$$

Note that Eq. (13) contains five equations: one conservation of mass equation, two conservation of momentum equations, one conservation of energy equation, and one Spalart–Allmaras turbulence model equation. Next, we write these equations at all subtime levels simultaneously, so that

$$\frac{\partial \boldsymbol{U}^{*}}{\partial t} + \frac{\partial \boldsymbol{F}^{*}}{\partial x} + \frac{\partial \boldsymbol{G}^{*}}{\partial y} = \boldsymbol{S}^{*} \tag{14}$$

where for example, $\boldsymbol{F}^{*}$ is the vector of x-fluxes evaluated at $\boldsymbol{U}^{*}$. Hence, Eq. (14) has $5 \times M$ equations.

Note that the M sets of conservation equations in Eq. (14) are coupled only through the time derivative term, which is approximated by the pseudospectral operator. To motivate the development of $\mathbf{D}$, we note that

$$\frac{\partial}{\partial t}\boldsymbol{U}^{*} = \sum_{k=1}^{K}[-\omega_k \cdot \mathbf{A}_k \sin(\omega_k t) + \omega_k \cdot \mathbf{B}_k \cos(\omega_k t)] \tag{15}$$

or in matrix form

$$\frac{\partial \boldsymbol{U}^{*}}{\partial t} = \frac{\partial \mathbf{E}}{\partial t}\tilde{\boldsymbol{U}} \tag{16}$$

Making use of Eq. (12) gives the desired pseudospectral operator,

$$\frac{\partial \boldsymbol{U}^{*}}{\partial t} = \frac{\partial \mathbf{E}}{\partial t}\mathbf{E}^{+}\boldsymbol{U}^{*} = \mathbf{D}\boldsymbol{U}^{*} \tag{17}$$

Finally, substitution of Eq. (17) into Eq. (14) gives the desired harmonic balance equations, i.e.,

$$\mathbf{D}\,\boldsymbol{U}^{*} + \frac{\partial \boldsymbol{F}^{*}}{\partial x} + \frac{\partial \boldsymbol{G}^{*}}{\partial y} = \boldsymbol{S}^{*} \tag{18}$$

Computational Scheme

Basic Scheme

In principle, n, l, and m can take on all integer values, generating an infinite number of frequencies and, therefore, subtime levels. In practice, only a few of the many possible frequencies contribute significantly to the nonlinear solution of the multistage flowfield. That is, as the number of spinning modes in the model is increased, the unsteady solution converges to a fixed solution, or at least the solution of the fundamental mode converges. This is called "modal convergence." We have found that good estimates of the unsteady flowfield can be obtained using a relatively small number of spinning modes.

The selection of the spinning modes is more art than science. However, there are some rules we follow. In case of the flutter problem, one should always include the fundamental mode, i.e., $(n, l, m) = (1, 0, 0)$. In addition, we usually select those spinning modes that have a relatively small number of nodal diameters, because low-order modes tend to be cut-on or weakly cutoff. We also try to include those modes with a large number of nodal diameters that are members of the fundamental mode's scatter group and provide a connection between the fundamental and low-order spinning mode. In case of the wake-interaction problem (no blade motion), one needs to set $n = 0$ for all spinning modes and pick different combinations of l and m.

The combinations (n, l, m) selected together with the values of initial frequency, initial interblade phase angle, the blade counts, and the rotational speed determine the number of frequencies in the solution, and hence the minimum number of subtime levels required. The minimum number of time levels for periodic flows is $M = 2K + 1$. For aperiodic flows, we usually keep about 50% more time levels than the minimum required, i.e., $M = 3K + 1$. Note that, in general, the final number of discrete frequency and interblade phase angle pairs will be fewer than the number of modes kept in the harmonic balance analysis. For example, assume that in the rotor frame we have two modes with $(n, l, m) = (1, -1, 0)$ and $(n, l, m) = (1, -1, 1)$. The first mode will have a frequency of $\omega_0 + B_1\Omega$ and an interblade phase angle of $2\pi(k_0 - B_1)/B_2$. Likewise, the second mode will have a frequency of $\omega_0 + B_1\Omega$ and an interblade phase angle of $2\pi(k_0 - B_1)/B_2 + 2\pi$. As one can see, the frequencies of these two modes are the same and their interblade phase angle differs by 2π. Therefore, one needs only one discrete set of frequency and interblade phase angles for these two modes. In this case, the zeroth tangential Fourier mode of the unsteady solution in the rotor row is coupled to the appropriate tangential mode of the stator row for mode 1. Note, however, when interrow coupling for mode 2 is performed, one needs to account for the 2π difference, and couple the first tangential Fourier mode.

Typically, the time levels are equally spaced over one representative period, but the time levels may be irregularly spaced. Indeed, when the flow is aperiodic, the conditioning of the $\mathbf{E}$ and $\mathbf{E}^{+}$ matrices may be improved by careful selection of the spacing. As an example, assume that for an aperiodic problem one has $K = 8$ discrete frequencies and interblade phase angles in a blade row. Therefore, we store the solution at $3K + 1$ time levels for the present method, hence Eq. (11) can be written in matrix-vector form as

$$\begin{Bmatrix} \boldsymbol{U}_1 \\ \boldsymbol{U}_2 \\ \boldsymbol{U}_3 \\ \vdots \\ \boldsymbol{U}_{25} \end{Bmatrix} = \underbrace{\begin{bmatrix} 1 & \cos\omega_1 t_1 & \cdots & \cos\omega_8 t_1 & \sin\omega_1 t_1 & \cdots & \sin\omega_8 t_1 \\ 1 & \cos\omega_1 t_2 & \cdots & \cos\omega_8 t_2 & \sin\omega_1 t_2 & \cdots & \sin\omega_8 t_2 \\ 1 & \cos\omega_1 t_3 & \cdots & \cos\omega_8 t_3 & \sin\omega_1 t_3 & \cdots & \sin\omega_8 t_3 \\ \vdots & & & & & & \\ 1 & \cos\omega_1 t_{25} & \cdots & \cos\omega_8 t_{25} & \sin\omega_1 t_{25} & \cdots & \sin\omega_8 t_{25} \end{bmatrix}}_{\mathbf{E}} \begin{Bmatrix} \mathbf{A}_0 \\ \mathbf{A}_1 \\ \vdots \\ \mathbf{A}_8 \\ \mathbf{B}_1 \\ \vdots \\ \mathbf{B}_8 \end{Bmatrix} \tag{19}$$

Having selected the time levels, we next solve Eq. (18). Note Eq. (18) is mathematically a "steady" equation, that is, time does not appear explicitly. So that the equations can be solved using conventional time-marching techniques, we introduce a pseudotime term [24], so that

$$\frac{\partial \boldsymbol{U}^{*}}{\partial \tau} + \mathbf{D}\boldsymbol{U}^{*} + \frac{\partial \boldsymbol{F}^{*}}{\partial x} + \frac{\partial \boldsymbol{G}^{*}}{\partial y} = \boldsymbol{S}^{*} \tag{20}$$

Equation (20) is then marched in pseudotime until convergence. When converged, the added pseudotime term goes to zero, and the harmonic balance equation [Eq. (18)] is recovered. Because only the steady-state solution of Eq. (20) is desired, acceleration techniques such as multiple-grid acceleration can be used to speed convergence.

Equation (20) is discretized on a computational grid spanning a single blade passage in each blade row. A typical (two-dimensional) grid is shown in Fig. 1 (every other computational node shown for

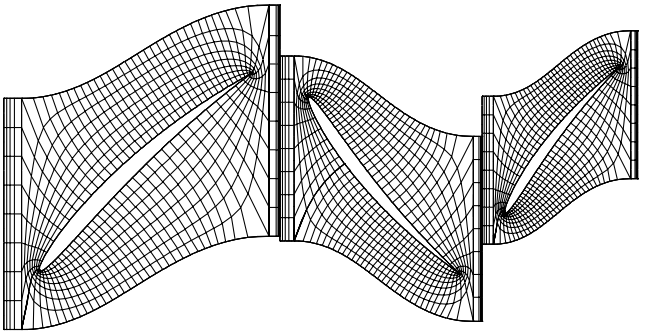

Fig. 1 Representative computational grid for a two-dimensional compressor (stator1/rotor2/stator2 of configuration D).

clarity). For the case shown here, the blade counts are in a ratio of 16:20:25. We use Ni's [25] Lax–Wendroff scheme to discretize the harmonic balance equations, with multiple-grid acceleration to speed convergence. Note the solution of the harmonic balance equations is similar to the solution of the steady Navier–Stokes equations. The vector of conservation variables, the flux vectors, and the vectors of source terms are somewhat larger, but the flux vectors and source terms are computed in the usual way at each time level. The equations at each time level are coupled together by the pseudospectral derivative term, which appears as an additional source term.

Periodicity Boundary Conditions

The computational domain can be reduced to a single blade passage within each blade row by making use of complex periodicity conditions along the periodic boundaries. To apply these conditions, the solution $\boldsymbol{U}^*$ is transformed along the periodic boundaries using Eq. (11) to find the vector of Fourier coefficients (which contains the cosine and sine coefficients $\mathbf{A}_k$ and $\mathbf{B}_k$). Inspection of Eqs. (7) and (8) reveals that the appropriate boundary condition is given by

$$\mathbf{A}_k(x, y+G) = \mathbf{A}_k(x, y) \cdot \cos(N_k G/R) - \mathbf{B}_k(x, y) \cdot \sin(N_k G/R) \tag{21}$$

$$\mathbf{B}_k(x, y+G) = \mathbf{A}_k(x, y) \cdot \sin(N_k G/R) + \mathbf{B}_k(x, y) \cdot \cos(N_k G/R) \tag{22}$$

These boundary conditions, similar to those developed by He and Denton [3,26] for time-accurate, time-marching flow solvers, are applied at every iteration of the Lax–Wendroff solver.

Multistage Coupling

At each iteration of the harmonic balance scheme, the solutions along the interrow boundaries of the computational grids are matched to one another. The process is as follows. The subtime level solutions $\boldsymbol{U}^*$ along the interrow boundaries of the rotor and stator passages are Fourier transformed in time using Eq. (10) to compute the temporal Fourier coefficients of the solution on the interrow boundaries. Next, a spatial Fourier transform in the tangential direction is performed on these coefficients to obtain the Fourier coefficients $\tilde{\mathbf{A}}_{nml}$ and $\tilde{\mathbf{B}}_{nml}$. These coefficients are then matched across the interrow boundaries. This matching is done for each tangential mode originally hypothesized as one of the (n, l, m) modes present in the solution. To eliminate spurious reflections off the interrow boundaries, two-dimensional nonreflecting boundary conditions are applied to those possible tangential modes *not* included in the hypothesized mode set. Thus, these higher tangential modes pass out of the computational domain and simply "disappear," that is, the outgoing waves do not influence the solution in the neighboring blade row, nor are they reflected back into the originating blade row.

Once the matching and nonreflecting boundary conditions have been applied to the Fourier coefficients $\tilde{\mathbf{A}}_{nml}$ and $\tilde{\mathbf{B}}_{nml}$, a spatial inverse Fourier transform is performed to find the temporal Fourier coefficients at each tangential node location along the interrow interface. Finally, a temporal inverse Fourier transform is performed [Eq. (11)] to determine the conservation variables $\boldsymbol{U}_i$ at each subtime level node.

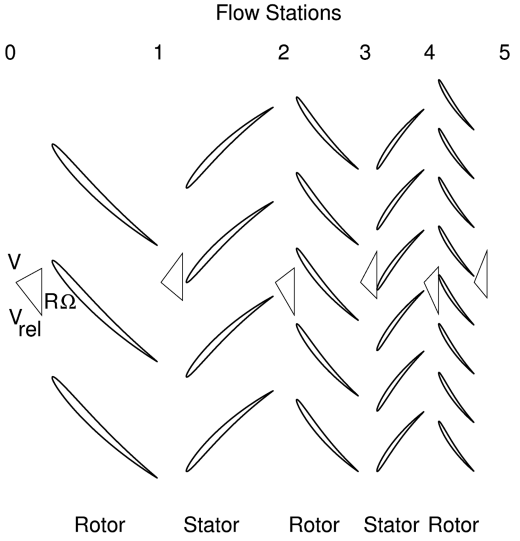

Fig. 2 Configuration D geometry.

Numerical Results

Inviscid Results

To validate the multistage harmonic balance method, we first compare computed two-dimensional small-amplitude multistage solutions to the time-linearized unsteady multistage analysis of Hall and Ekici [23] and Silkowski and Hall [27]. Specifically, we consider here configuration D, a model two-dimensional compressor geometry. This configuration, shown in Fig. 2, is composed of five rows (rotor1/stator1/rotor2/stator2/rotor3) of NACA four-digit series airfoils; details of this configuration are given in Table 1. The lengths are nondimensionalized here by the aerodynamic chord of the rotor blades in the middle row, velocities by the relative inflow velocity at station 2, and the pressures by the dynamic pressure at station 2.

For the first case, we consider the middle three blade rows (stator1/rotor2/stator2). Shown in Fig. 3 is the mean pressure on the surface of the reference rotor airfoil computed using the present flow solver. Also shown in the same figure is the computation from the coupled mode method (CMM) of Silkowski and Hall [27]. As one can see, the agreement for the two flow solvers is very good for the steady-state solution.

Next, the rotor blades are prescribed to vibrate in plunge normal to the blade chord with a small-amplitude at a reduced frequency of 0.5, and an interblade phase angle of 60.0 deg. Using the present harmonic balance (HB) method, we computed the resulting unsteady multistage flow. For this initial case, we coupled the solutions using just two tangential modes, the zero nodal diameter mode (steady flow coupling), and the fundamental tangential mode associated with an interblade phase angle of 60.0 deg. For these computations, three subtime levels were used.

Figure 4 shows the real and the imaginary (in-phase and out-of-phase) parts of the first harmonic of the unsteady surface pressure of the reference rotor computed using the present method. Also shown for comparison are the results of the time-linearized multistage Euler analysis of Hall and Ekici [23]. Note the unsteady pressure is normalized here by $j\omega_0 \rho U h_0$, where ρ and U are the density and the relative velocity at flow Station 2, respectively, and h_0 is the plunging amplitude of blades of the middle row. It can be seen that the present method and the previous time-linearized method of Hall and Ekici are in virtually exact agreement, indicating that for small-disturbance flows the present method correctly predicts the unsteady flow, including the effects of multistage coupling. Also shown in Fig. 4 is the unsteady surface pressure computed for the rotor alone, without

Table 1 Geometric and fluid dynamic parameters for configuration D

Row or flow station	0	1	2	3	4	5
Number of blades	——	26	32	40	50	62
NACA 4-digit airfoil	——	(3.5)506	(4.5)506	(4.5)506	(4.5)506	(4.5)506
Chord	——	1.539	1.25	1.0	0.8	0.645
Blade-to-blade gap, G	——	1.231	1.0	0.8	0.64	0.516
Axial gap	——	0.31	0.25	0.20	0.16	——
Relative velocity	1.112	0.744	1.000	0.609	0.919	0.531
Absolute velocity	0.780	0.959	0.630	0.926	0.562	0.906
Relative Mach	0.829	0.535	0.700	0.414	0.609	0.344
Absolute Mach	0.581	0.689	0.441	0.629	0.373	0.586
Relative flow angle	−52.0	−40.0	−60.0	−45.0	−65.5	−50.5
Absolute flow angle	28.6	53.5	37.5	62.3	47.3	68.1
Stagger angle	——	−44.0	43.0	−49.5	52.0	−55.0
Static pressure	0.939	1.213	1.458	1.797	2.131	2.524
Relative total pressure	1.473	1.473	2.022	2.022	2.739	2.739
Absolute total pressure	1.180	1.666	1.666	2.346	2.346	3.185

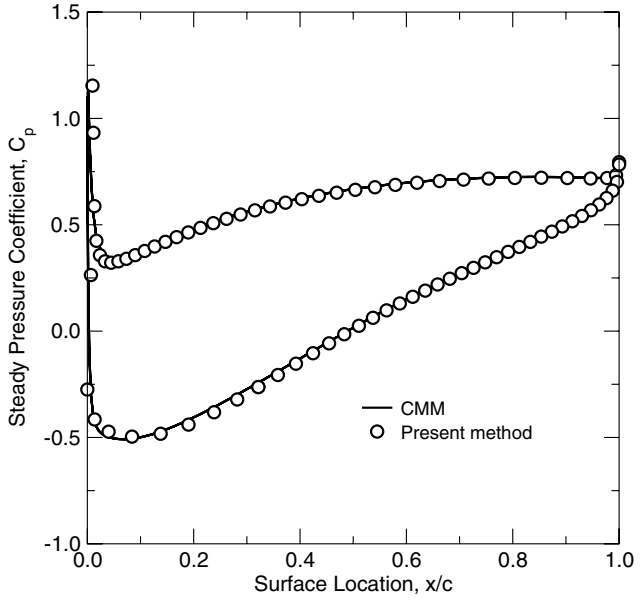

Fig. 3 Mean pressure distribution on the reference rotor blade of configuration D.

the influence of the neighboring stators. One sees that the presence of the neighboring stator blade rows substantially changes the unsteady pressure distribution on the rotor blades.

Next, we varied the interblade phase angle between −180 and 180 deg and computed the unsteady lift using the present method, again for small-amplitude vibrations with just two tangential modes (three subtime levels) used to couple the blade rows. Figure 5 shows the real and imaginary parts of the unsteady lift computed using the present harmonic balance method. Also shown for comparison is the CMM of Silkowski and Hall [27], a frequency-domain multistage analysis based on the time-linearized full potential equations. The lift is nondimensionalized by $j\omega\rho U h_0 c$. With this nondimensionalization, the aerodynamic damping is proportional to the real part of the computed unsteady lift; in regions where the real part of the unsteady lift is positive, the aerodynamic damping is negative, and thus the blades will flutter. Note the present multistage harmonic balance analysis and the CMM method are in very good agreement over the full range of interblade phase angles.

Also shown in Fig. 5 is the unsteady lift computed without the influence of the neighboring stators. Again, we see that the multistage effects can significantly affect the unsteady aerodynamic response of a row of vibrating rotor blades. To understand the relative importance of the upstream and downstream stators, we recomputed the unsteady lift on the rotor blades, but this time with only the

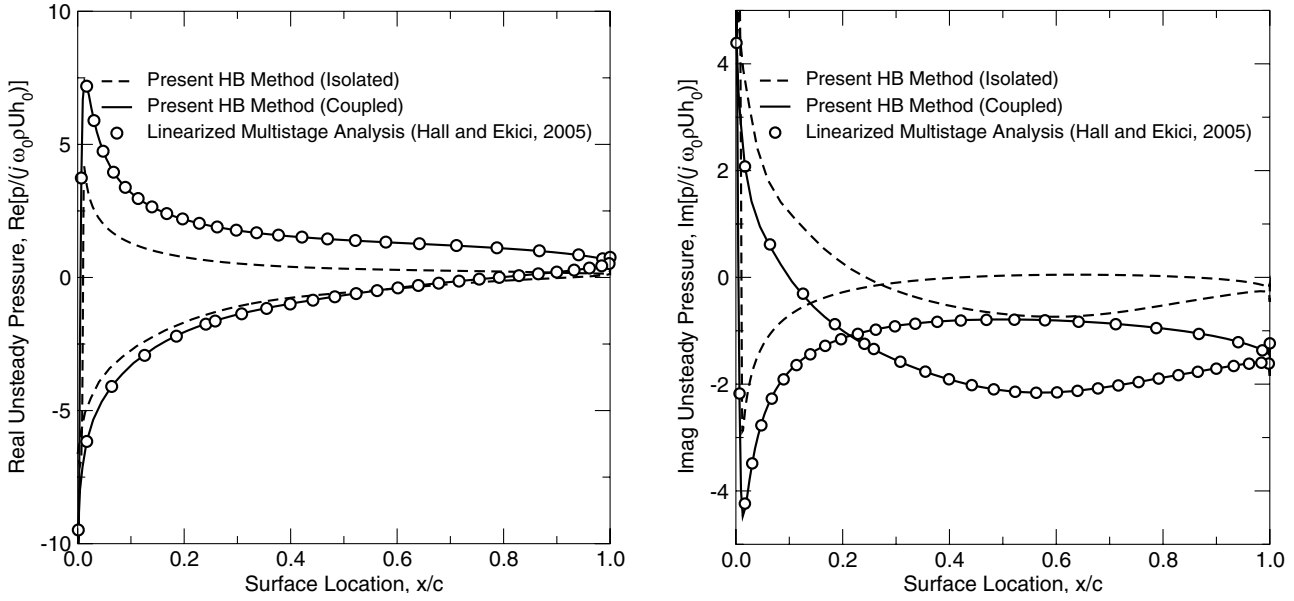

Fig. 4 Real and imaginary part of unsteady pressure on the reference rotor blade of configuration D. For the harmonic balance computations, $K = 1$, $M = 3$.

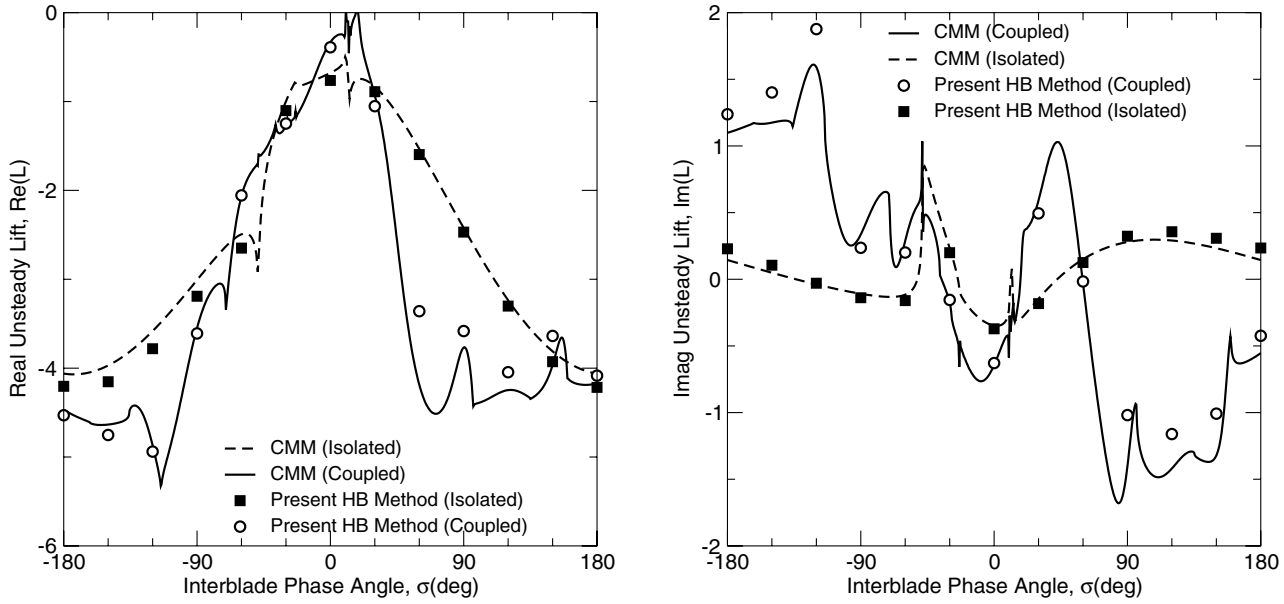

Fig. 5 Computed real and imaginary unsteady lift acting on the reference rotor blade of configuration D. For the harmonic balance computations, $K = 1, M = 3$.

upstream stator or the downstream stator present. These results are shown in Fig. 6. One observes that the stator1/rotor2/stator2 results agree more closely with the rotor2/stator2 computation than the stator1/rotor2 computation. Note that in more realistic viscous cases, one would expect the upstream blade row to have a more pronounced effect than the downstream blade row. However, for this inviscid example, the downstream stator row has a more pronounced influence on the unsteady aerodynamic response of the rotor than does the upstream stator.

Note that in all the multistage results presented thus far, the "first harmonic" of the unsteady lift at an interblade phase angle of -180 deg is not equal to the unsteady lift at an interblade phase angle of $+180$ deg. This result is incorrect, as physically these interblade phase angles correspond to the same prescribed blade motion. The problem is that only two tangential modes were used to couple the blade rows when physically several modes play an important role in the multistage coupling. Hall and Silkowski [27] showed the correct interblade phase angle periodicity can be achieved by including more tangential modes in their CMM model; we expect the same will hold for the present multistage harmonic balance analysis. Furthermore, the results shown thus far are for small-disturbance unsteady flows, flows in which nonlinear effects are relatively unimportant.

To explore some of these effects, we consider again the rotor2/stator2 case shown in Fig. 6. These results were recomputed for the same conditions for both small-amplitude and large-amplitude vibratory motions. In the small-amplitude case, the amplitude of blade vibration is 0.001 times the chord; in the large-amplitude case, the vibration amplitude is 0.03 times the chord. For both cases, we use 27 (n, l, m) modes, resulting in eight discrete frequencies in each frame of reference. A total of 25 subtime levels were used in the harmonic balance analysis. Figure 7 shows the computed unsteady lift (at the frequency of the blade vibration) for these cases, together with the two-mode case presented earlier. Note that for the small-amplitude case, the 27-mode and the two-mode models are in very good agreement over most of the interblade phase angle range. However, near an interblade phase angle of $+180$ deg, the 27-mode model results begin to differ, and (we presume) are more accurate. Note for example that the 27-mode results are periodic, that is, the unsteady lift is now very nearly equal at $\sigma = \pm 180$ deg.

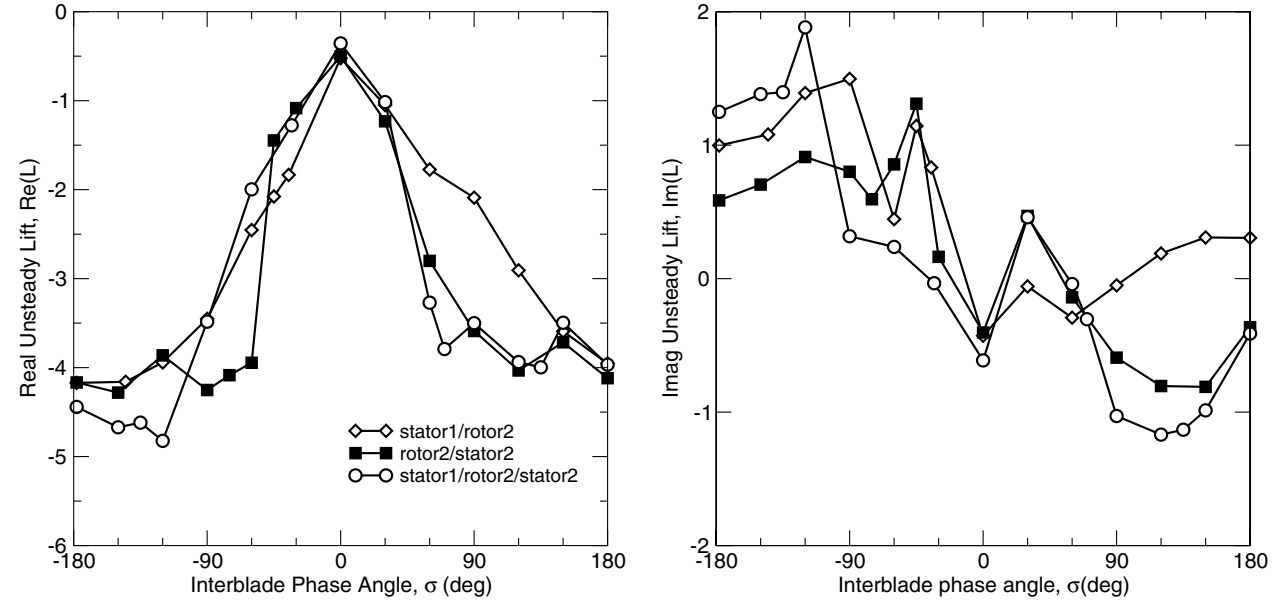

Fig. 6 Computed real and imaginary unsteady lift acting on the reference rotor blade of configuration D. For the harmonic balance computations, $K = 1, M = 3$.

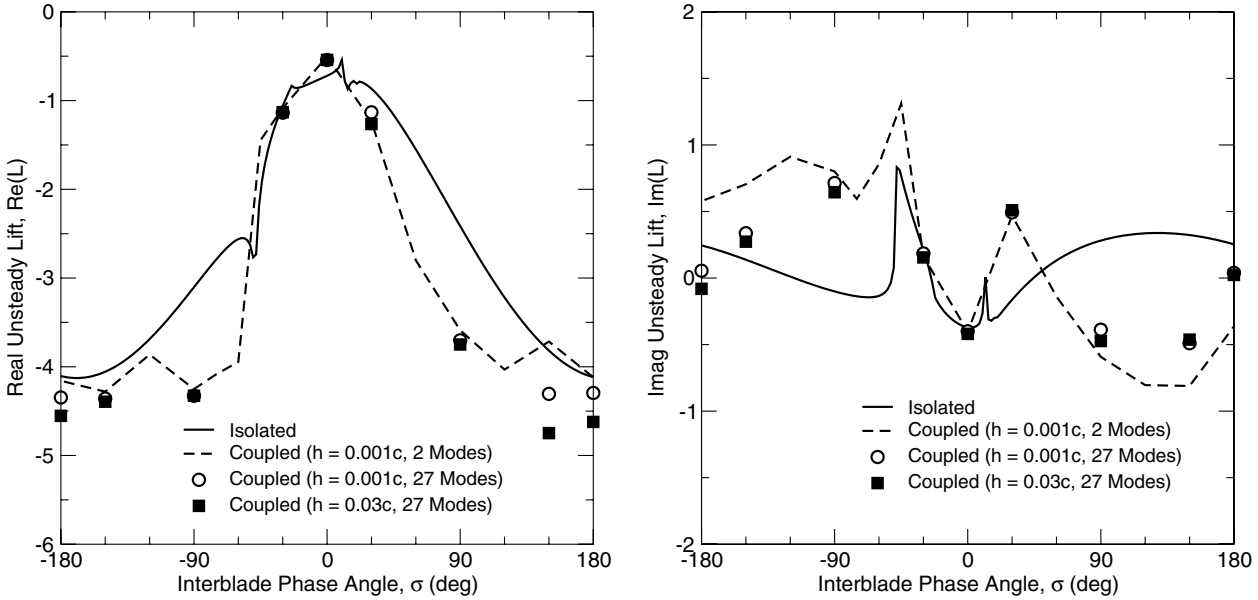

Fig. 7 Computed real and imaginary unsteady lift acting on the reference rotor blade of configuration D. For the 27-mode case, $K = 8$ and $M = 25$. For the two-mode case, $K = 1$ and $M = 3$.

Also shown in Fig. 7 are the computed lifts for a relatively large-amplitude blade vibration ($h = 0.03c$). We see that over most of the interblade phase angle range, the nondimensional lift is insensitive to amplitude. However, for interblade phase angles near 180 deg, there are some modest but significant differences between the small-amplitude and large-amplitude lifts, indicating the presence of nonlinear effects.

Finally, we consider this same rotor2/stator2 case, but now the rotor blades vibrate with a reduced frequency ω_0 of 1.0 with an interblade phase angle of 90 deg and an amplitude equal to 0.03 times the chord. Shown in Fig. 8 is a contour plot showing the pressure field within the stage. Note that the computational passage spans only a single passage in each blade row. The solution is reconstituted and plotted on multiple passages here for clarity. One can clearly see the unsteady interaction of the (steady) pressure field around the leading edge of the downstream stator with the aft region of the upstream rotor. What is less clear is whether this interaction affects the unsteady pressure distribution on the rotor surface at the frequency of the blade vibration.

Figure 9 shows the unsteady pressure on the surface of the reference rotor blade (at the blade vibratory frequency) for three cases. Shown is the pressure distribution for the rotor in isolation (uncoupled from the stator), and also with the stator present. For the latter coupled case, two slightly different sets of tangential modes were used to couple the rotor and stator. In one case, only $l = 0$ modes were used for modes where $n = 0$; in the other case, $l = 0$ and $l = \pm 1$ modes were used. In other words, in the first case, the upstream rotor only sees a tangential average of the mean flow about the downstream stator; in the second case, the rotor sees the unsteadiness at the stator passing frequency due to the pressure variation around the leading edge of the stator. Note both the coupled cases have nearly identical pressure distributions (both of which are significantly different than the pressure distribution for a rotor in isolation). These results indicate that there is no significant nonlinear interaction between the unsteadiness in the flow associated with blade vibration and the unsteadiness associated with stator passing, at least for this example. We would expect that important nonlinear effects may be present for stronger interactions, as in the case of shock/rotor interactions seen in high speed turbine stages, or strong wake/rotor interactions.

Viscous Results

In this section, we investigate how the current method reacts to the forced response problem. Here, we consider the middle three blade rows of configuration D (stator1/rotor2/stator2). At the inlet, we specify the same boundary conditions as the inviscid case, i.e., $P_{t_{\text{abs}}} = 1.666$, $T_{t_{\text{abs}}} = 1.515$, and $\alpha_{\text{abs}} = 53.5$. At the exit, however, we specify a lower static pressure ($P_{\text{exit}} = 1.458$) compared with the inviscid case. For a lower back pressure, the steady viscous solution is somewhat similar to the inviscid solution.

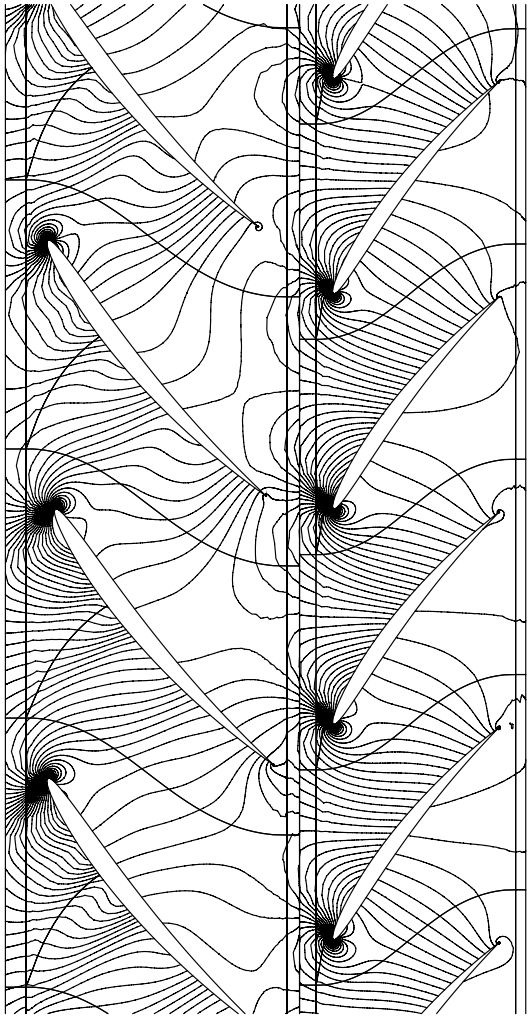

Fig. 8 Computed pressure in rotor2/stator2 of configuration D.

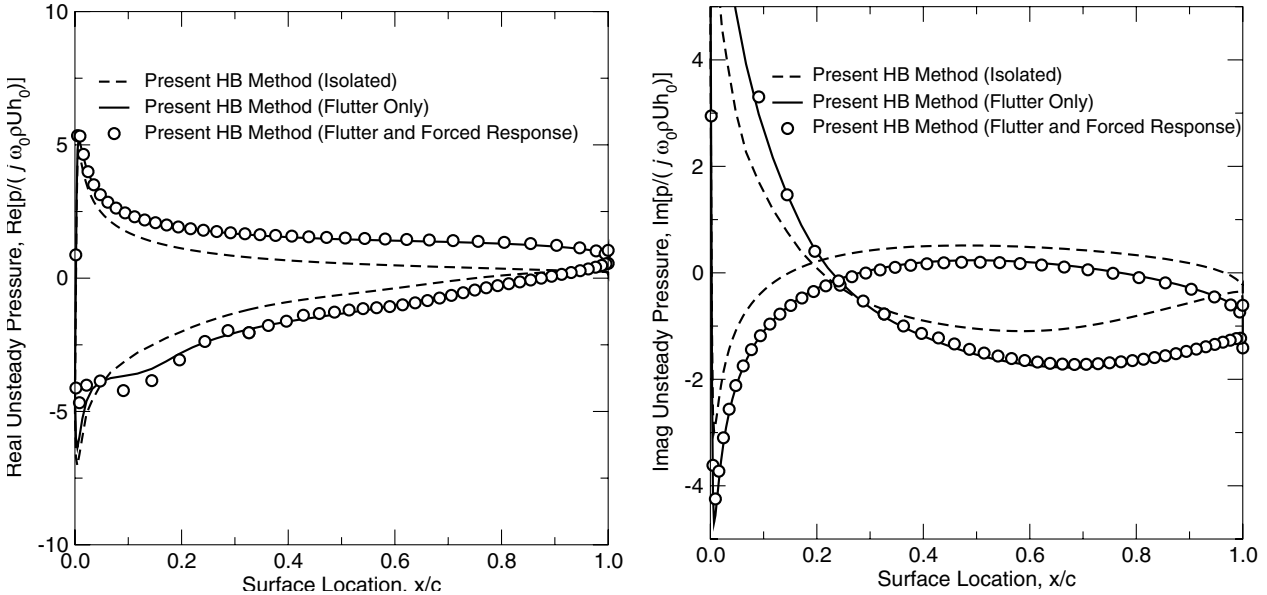

Fig. 9 Computed real and imaginary unsteady lift acting on the reference rotor blade of configuration D. For the harmonic balance computations, $K = 6$ and $M = 19$ (flutter mode coupling only) or $K = 7$ and $M = 22$ (flutter and stator passing coupling).

For this case, none of the blade rows vibrate and thus the main source of unsteadiness is the upstream blade row viscous wakes. For a pure wake-interaction problem, one needs to set $n = 0$ and pick different combinations of (l, m, i). For this case, we used eight and 27 (n, l, m, i) combinations [in the eight-mode case we pick all possible combinations of 0 and 1, and in the 27-mode case we pick all possible combinations of 0, 1, and 2 for (l, m, i)] for the present method. This results in three and eight discrete frequencies and interblade phase angles in each frame of reference for eight and 27 modes, respectively.

Figure 10 shows the real and imaginary parts of the unsteady pressure on the middle rotor row at the upstream stator passing frequency. The unsteady pressure was nondimensionalized by the mean $\rho U V_R$ value at flow station 2. As one can see, the pressure distribution for eight and 27 modes are relatively close to each other. This shows that a good approximation for the unsteady solution can be obtained using as few as eight modes in the model.

Shown in Fig. 11 are the computed instantaneous contour plots of entropy and pressure for a 27-mode harmonic balance method. Note that all computations were performed on a grid that spans only a single blade passage in each blade row. The solution was reconstituted and plotted on multiple passages for clarity. As one can see, the current method allows wakes to pass smoothly from one blade row to the other (see Fig. 11a). Also note that the wake from stator1 travels downstream to stator2 and interacts with the wake from the rotor row. In addition, Fig. 11a clearly shows the unsteady interaction of the pressure field around the leading edge of the downstream blade rows with the aft region of the upstream blade rows.

These results indicate that our method can be used for investigating the viscous wake/rotor interaction as well as the potential interaction between the neighboring blade rows in two-dimensional configurations.

Conclusions

In this paper, we have presented a new harmonic balance technique for computing unsteady flows in multistage turbomachinery. Our method can be used for investigating the viscous wake/

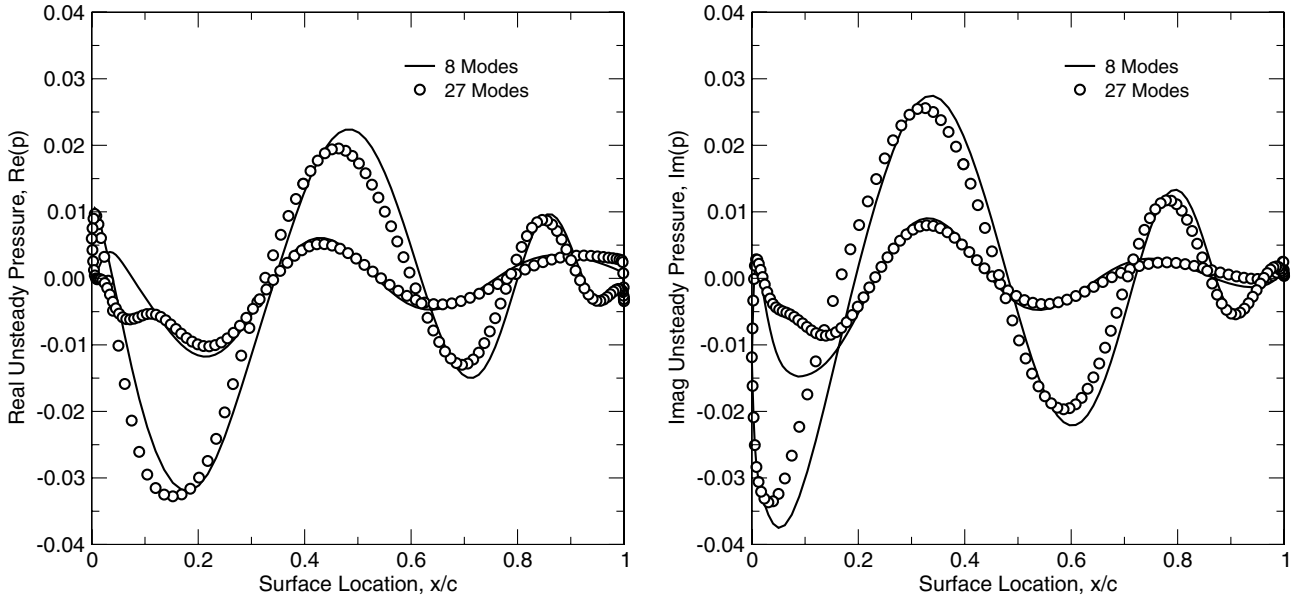

Fig. 10 Computed real and imaginary unsteady pressure at the stator1 passing frequency on the reference rotor blade of configuration D. For eight modes, $K = 3$ and $M = 10$; for 27 modes, $K = 8$ and $M = 25$.

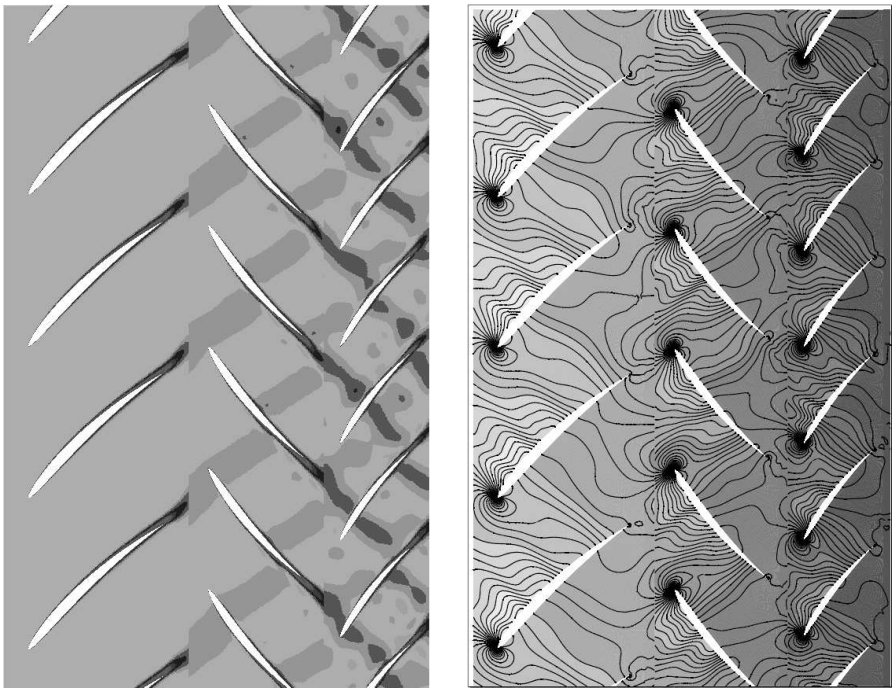

a) Instantaneous entropy contours b) Instantaneous pressure contours

Fig. 11 Computed unsteady solution in stator1/rotor2/stator2 of configuration D. For 27 modes, $K = 8$ and $M = 25$.

rotor interaction as well as the potential interaction between the neighboring blade rows in two-dimensional configurations. The method, which is particularly well suited for the computation of the aerodynamic forces that produce flutter and forced response in turbomachinery, can model flow nonlinearities and aperiodic flows. The method uses a computational domain spanning a single blade passage in each blade row, with a small number of subtime level solutions stored in each blade row. We have shown that accurate unsteady pressure loads can be computed using a small number of subtime level solutions. Thus, the method is computationally very efficient, requiring CPU times that scale like the number of subtime levels in the model times the cost of a single steady flow calculation. Furthermore, because the problem is cast in a mathematically steady-state form, with unsteady frequencies appearing as parameters, the formulation is well suited for use with adjoint sensitivity analyses. Finally, although the method was presented for two-dimensional flows, it is easily generalized to three-dimensional cases (our computer code implementation incorporates both two- and three-dimensional Euler/Navier–Stokes equations).

Acknowledgments

This work was sponsored by a grant from the NASA John H. Glenn Research Center (NASA Grant NAG3-2627) with technical oversight provided by Anatole Kurkov. Additional support was provided by the GUIde Consortium, with technical oversight provided by Jerry Griffin of Carnegie Mellon University. The authors gratefully acknowledge the helpful comments of Steven R. Hall of the Massachusetts Institute of Technology regarding the use of pseudoinverses.

References

[1] Hall, K. C., and Crawley, E. F., "Calculation of Unsteady Flows in Turbomachinery Using the Linearized Euler Equations," *AIAA Journal*, Vol. 27, No. 6, June 1989, pp. 777–787.

[2] Clark, W. S., and Hall, K. C., "Time-Linearized Navier–Stokes Analysis of Stall Flutter," *Journal of Turbomachinery*, Vol. 122, July 2000, pp. 467–476.

[3] He, L., and Denton, J. D., "Three-Dimensional Time-Marching Inviscid and Viscous Solutions for Unsteady Flows Around Vibrating Blades," *Journal of Turbomachinery*, Vol. 116, No. 3, July 1994, pp. 469–476.

[4] Hall, K. C., "Computation of Unsteady Nonlinear Flows in Cascades Using a Harmonic Balance Technique," presented at the Kerrebrock Symposium, *A Symposium in Honor of Professor Jack L. Kerrebrock's 70th Birthday*, Massachusetts Inst. of Technology, Cambridge, MA, Jan. 1998.

[5] Hall, K. C., Thomas, J. P., and Clark, W. S., "Computation of Unsteady Nonlinear Flows in Cascades Using a Harmonic Balance Technique," *AIAA Journal*, Vol. 40, No. 5, May 2002, pp. 879–886.

[6] Giles, M. B., "Approach for Multi-Stage Calculations Incorporating Unsteadiness," American Society of Mechanical Engineers Paper 92-GT-282, 1992.

[7] He, L., and Ning, W., "Efficient Approach for Analysis of Unsteady Viscous Flows in Turbomachines," *AIAA Journal*, Vol. 36, No. 11, Nov. 1998, pp. 2005–2012.

[8] Ning, W., and He, L., "Computation of Unsteady Flows Around Oscillating Blades Using Linear and Non-Linear Harmonic Euler Methods," *Journal of Turbomachinery*, Vol. 120, No. 3, 1998, pp. 508–514.

[9] Davis, R. L., Shang, T., Buteau, J., and Ni, R. H., "Prediction of 3-D Unsteady Flow in Multi-Stage Turbomachinery Using an Implicit Dual Time-Step Approach," AIAA Paper 96-2565, 1996.

[10] McMullen, M., Jameson, A., and Alonso, J. J., "Acceleration of Convergence to a Periodic Steady State in Turbomachinery Flows," AIAA Paper 2001-152, 2001.

[11] McMullen, M., Jameson, A., and Alonso, J. J., "Application of a Non-Linear Frequency Domain Solver to the Euler and Navier–Stokes Equations," AIAA Paper 2002-120, 2002.

[12] Nadarajah, S., McMullen, M., and Jameson, A., "Optimal Control of Unsteady Flows Using Time Accurate and Non-Linear Frequency Domain Methods," AIAA Paper 2003-3875, 2003.

[13] van der Weide, E., Gopinath, A., and Jameson, A., "Turbomachinery Applications with the Time Spectral Method," AIAA Paper 2005-4905, 2005.

[14] Thomas, J. P., Dowell, E. H., and Hall, K. C., "Nonlinear Inviscid Aerodynamic Effects on Transonic Divergence, Flutter, and Limit-Cycle Oscillations," *AIAA Journal*, Vol. 40, No. 4, April 2002, pp. 638–646.

[15] Thomas, J. P., Hall, K. C., and Dowell, E. H., "Harmonic Balance Approach for Modeling Nonlinear Aeroelastic Behavior of Wings in Transonic Viscous Flow," AIAA Paper 2003-1924, 2003.

[16] Thomas, J. P., Hall, K. C., Dowell, E. H., and Denegri, C., "Modeling Limit Cycle Oscillation Behavior of the F-16 Fighter Using a Harmonic Balance Approach," AIAA Paper 2004-1696, 2004.

[17] Thomas, J. P., Hall, K. C., Dowell, E. H., and Denegri, C., "Further

Investigation of Modeling Limit Cycle Oscillation Behavior of the F-16 Fighter Using a Harmonic Balance Approach," AIAA Paper 2005-1917, 2005.

[18] Thomas, J. P., Hall, K. C., and Dowell, E. H., "Discrete Adjoint Approach for Modeling Unsteady Aerodynamic Design Sensitivities," *AIAA Journal*, Vol. 43, No. 9, Sept. 2005, pp. 1931–1936.

[19] Welch, G., Milanovic, I., and Zaman, K., "Application of Harmonic Balance Technique to Synthetic Jets in Cross-Flow," AIAA Paper 2005-1111, 2005.

[20] Breard, C., "Acoustic Propagation and Radiation Modeling of Lined Duct with Linear and Non-Linear Frequency-Domain Solver," AIAA Paper 2003-3265, 2003.

[21] He, L., Chen, T., Wells, R. G., Li, Y. S., and Ning, W., "Analysis of Rotor-Rotor and Stator-Stator Interferences in Multi-Stage Turbomachines," *Journal of Turbomachinery*, Vol. 124, No. 4, Oct. 2002, pp. 564–571.

[22] Spalart, P. R., and Allmaras, S. R., "One-Equation Turbulence Model for Aerodynamic Flows," AIAA Paper 92-0439, 1992.

[23] Hall, K. C., and Ekici, K., "Multistage Coupling for Unsteady Flows in Turbomachinery," *AIAA Journal*, Vol. 43, No. 3, March 2005, pp. 624–632.

[24] Ni, R. H., and Sisto, F., "Numerical Computation of Nonstationary Aerodynamics of Flat Plate Cascades in Compressible Flow," *Journal of Engineering for Power*, Vol. 98, No. 2, April 1976, pp. 165–170.

[25] Ni, R. H., "Multiple-Grid Scheme for Solving the Euler Equations," *AIAA Journal*, Vol. 20, No. 11, Nov. 1982, pp. 1565–1571.

[26] He, L., "Circumferential Phase-Shift Condition for Turbomachinery Aerodynamic and Aeromechanical Applications," AIAA Paper 2005-16, 2005.

[27] Silkowski, P. D., and Hall, K. C., "Coupled Mode Analysis of Unsteady Multistage Flows in Turbomachinery," *Journal of Turbomachinery*, Vol. 120, No. 3, July 1998, pp. 410–421.

S. Aggarwal
Associate Editor